Article

Two-dimensional Mxenes Mo2Ti2C3Tz and Mo2TiC2Tz: microscopic conductivity and dynamics of photoexcited carriers

GUANGJIANG LI, Varun Natu, Teng Shi, Michel W Barsoum, and Lyubov V. Titova

ACS Appl. Energy Mater., **Just Accepted Manuscript** • DOI: 10.1021/acsaem.9b01966 • Publication Date (Web): 13 Jan 2020

Two-dimensional MXenes $Mo_2Ti_2C_3T_z$ and $Mo_2TiC_2T_z$: microscopic conductivity and dynamics of photoexcited carriers

Guangjiang Li[1,*], Varun Natu[2,*], Teng Shi[1], Michel W. Barsoum[2] and Lyubov V. Titova[1**]

[1]Department of Physics, Worcester Polytechnic Institute, Worcester MA 01609

[2]Department of Materials Science and Engineering, Drexel University, Philadelphia, PA 19104

* *These authors contributed equally*

** Corresponding author: ltitova@wpi.edu

MXenes are a recently discovered family of two-dimensional transition metal carbides, nitrides and carbonitrides with electronic properties that can be tuned by their chemistry and structure. Herein THz spectroscopy was used to investigate the microscopic conductivity and photoexcited charge carrier dynamics in two Mo-based MXenes: $Mo_2Ti_2C_3T_z$ and $Mo_2TiC_2T_z$. We find that both have high intrinsic carrier densities (~ 10^{20} cm^{-3} in $Mo_2Ti_2C_3T_z$ and ~ 10^{19} cm^{-3} in $Mo_2TiC_2T_z$) and mobilities, and exhibit high conductivities within individual nanosheets. Optical excitation results in a transient conductivity increase in both compositions, in stark contrast with the most studied member of MXene family, $Ti_3C_2T_z$, where photoexcitation suppresses conductivity for nanoseconds. De-intercalation of water and other species from between the nanosheets by mild vacuum annealing further improves the long-range, inter-nanosheet transport of the photoexcited carriers and increases their lifetime. High and long-lived photoinduced conductivity that can be engineered by substituting Mo for Ti render the Mo-based MXenes attractive for a variety of optoelectronic, sensing and photoelectrochemical applications.

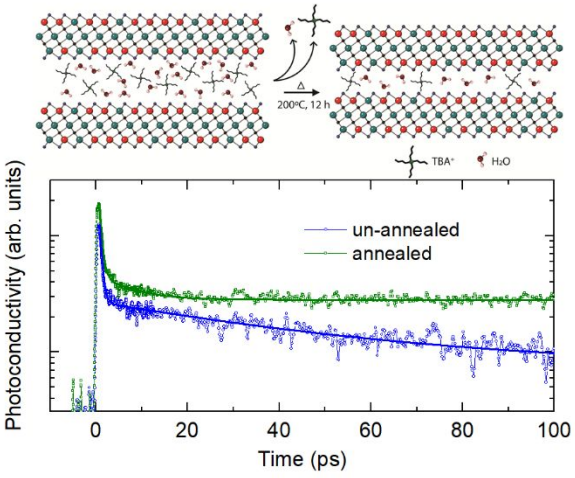

1. Introduction

MXenes are an emergent family of 2D transition metal transition metal carbides, nitrides and carbonitrides with the general formula $M_{n+1}X_nT_z$, where M is an early transition metal, X is carbon and/or a nitrogen, and n is 1, 2, or 3. T_z stands for a surface termination, e.g., –OH, –F, =O. Their electronic properties have been predicted to span the range from highly conductive metallic to semimetallic, semiconducting and even topologically insulating[1-7].

Some MXenes exhibit phenomena such as record high volumetric capacitance and optical nonlinearity, suggesting that they can find use in charge storage, transparent flexible conductors, electromagnetic shielding and nonlinear optical devices[8-17]. This wide variety of properties and potential applications underscores the need to understand the mechanisms of carrier transport in these new materials as a function of their chemical composition, terminations and processing method.

To fabricate MXenes, the A element such as Al is removed from a parent MAX phase, typically by etching, mostly in F-containing aqueous media. During the etching process, the A layers are replaced by the surface terminations, T_z. Once a typically aqueous colloidal suspension of MXene is formed, films can be readily formed from the latter by coating them on substrates. In these films, water molecules and cations occupy the space between individual MXene nanosheets and can affect transport properties, such that removing them by annealing can sometimes lead to dramatic changes in transport properties[1, 7]. The transport properties of MXene films result from a complicated interplay of intra-nanosheet carrier transport determined mainly by the properties of the $M_{n+1}X_n$ cores and affected by their point and other defects, and long-range, inter-nanosheets transport. The latter carrier motion is sensitive not only to the nature of T_z, but also to the properties of the nanosheet edges and any species intercalated between the nanosheets.

Titanium carbide MXene $Ti_3C_2T_z$ was the first discovered and has since been the most extensively studied. Studies have demonstrated that not only are individual $Ti_3C_2T_z$ MXenes flakes metallic with a high carrier density and mobility, consistent with DFT calculations that predict high density of states at the Fermi level E_F, but macroscopic $Ti_3C_2T_z$ films retain metallic-like conductivity with positive dR/dT over a broad temperature range[3, 7]. The metallicity is also evidenced by single nanosheet measurements[18].

The situation is more complicated in molybdenum, Mo-based MXenes. While

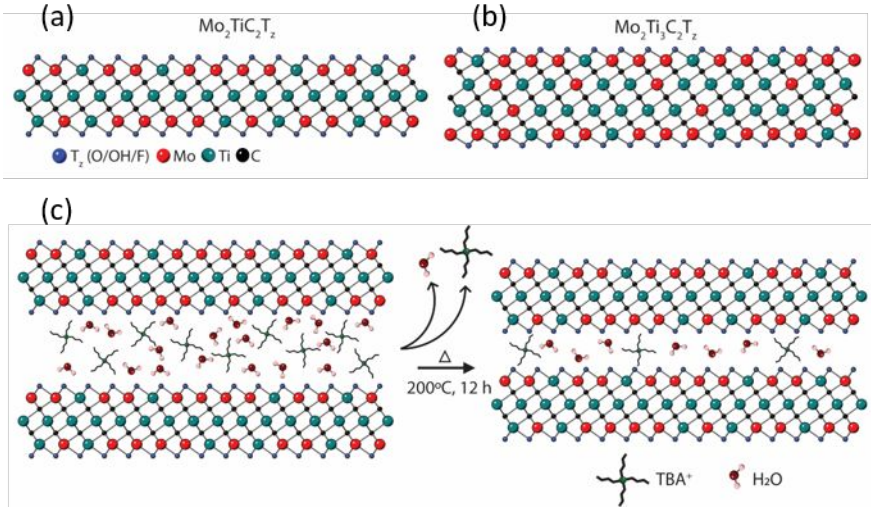

Figure 1. Schematic depiction of (a) $Mo_2TiC_2T_z$ and (b) $Mo_2Ti_2C_3T_z$ structure. (c) Effect of vacuum annealing on a film structure and inter-nanosheet distance.

non-spin-polarized DFT calculations predict them to be metallic with significant DOS at the E_F,[19] accounting for spin polarization opens of a small (tens of meV) gap in –OH and –F terminated Mo-MXenes but not in O-terminated Mo-MXenes[3].

Experiments have shown that replacing some or all of Ti with Mo in a MXene structure results in a lower carrier density, and a semiconductor-like behavior has been reported in several studies of multi-layer Mo-MXene films as resistivity showed a slow increase at lower temperatures (dR/dT<0)[1, 3, 7, 19]. However, systematic temperature-dependent magneto-transport measurements of Mo-based MXenes revealed that they behave like disordered systems, not unlike granular metals. Their long-range conductivity is limited by the *inter-nanosheet* carrier transfer which occurs mainly by variable range hopping (VRH), with a contribution from a thermally-activated mechanism at higher temperatures[1]. These experiments also demonstrated that conductivity is strongly dependent on inter-nanosheet distance, and increases by orders of magnitude when annealing reduces this distance by releasing the water and other intercalants from the inter flake space. Finally, vacuum annealing (up to 775 °C) $Mo_2TiC_2T_z$ at temperatures that are sufficiently high to eliminate most intercalated species was found to reverse the sign of dR/dT from negative to positive (metallic-like), establishing the intra-nanosheet metallicity of $Mo_2TiC_2T_z$, and demonstrating that the dR/dT<0 behavior of multi-layer Mo-MXenes is most probably caused by the inter-nanosheet species.[7] However, an exact picture of the microscopic conductivity and charge carrier dynamics in Mo-MXenes, remains incomplete.

Terahertz (THz) spectroscopy, an all-optical, non-contact probe of microscopic conductivity, equilibrium and non-equilibrium free carrier dynamics, can provide just the insight needed for a comprehensive picture of the transport properties over microscopic length scales.[20-21] With the THz pulse bandwidth of 0.25 – 2.1 THz (or, equivalently, 1-10 meV in terms of photon energy), free carrier absorption results in attenuation of the THz probe pulse transmitted through a MXene film, and the strength of this absorption is governed by the free carrier density and mobility. THz spectroscopy yields a frequency-resolved complex conductivity without the complication of electrical contacts. It is sensitive to the carrier motion on length scales, L of tens to hundreds of nanometers, determined by the probing THz frequency ω according to $L(\omega) \propto (D/\omega)^{1/2}$, where D is the diffusion constant.[22-23] THz conductivity spectra thus represent microscopic carrier transport, averaged over many nanosheets present in ~ a 1 to 2 mm diameter THz probe spot size.[24] Lastly, time-resolved THz spectroscopy (TRTS) takes advantage of the short duration of THz pulses to examine the effects of photoexcitation on conductivity and carrier dynamics with sub-picosecond, ps, time resolution[20, 25-29]. In metals, changes in conductivity in response to optical excitation include contributions of both intra-band free carrier absorption and inter-band transitions which can introduce additional free carriers if the excitation energy is higher than the inter-band transition threshold.[30]

Recently, we reported on the THz spectroscopic study of a metallic $Ti_3C_2T_z$ MXene film. We found that it has a high, ~ 2×10^{21} cm^{-3} intrinsic charge carrier density, relatively high (~34 cm^2/Vs) mobility of carriers *within* individual $Ti_3C_2T_z$ nanosheets, and a long-range mobility of ~ 1 cm^2/Vs, limited by inter-nanosheet transport.[15] In this metallic MXene, photoexcitation with 100 fs duration, 800 nm laser pulses induces transient suppression of conductivity, which recovers over hundreds of ps. The transient suppression is believed to be due to the excitation-induced

reduction in mobility of existing free carriers playing a more important role that a small increase in carrier density by inter-band excitation.

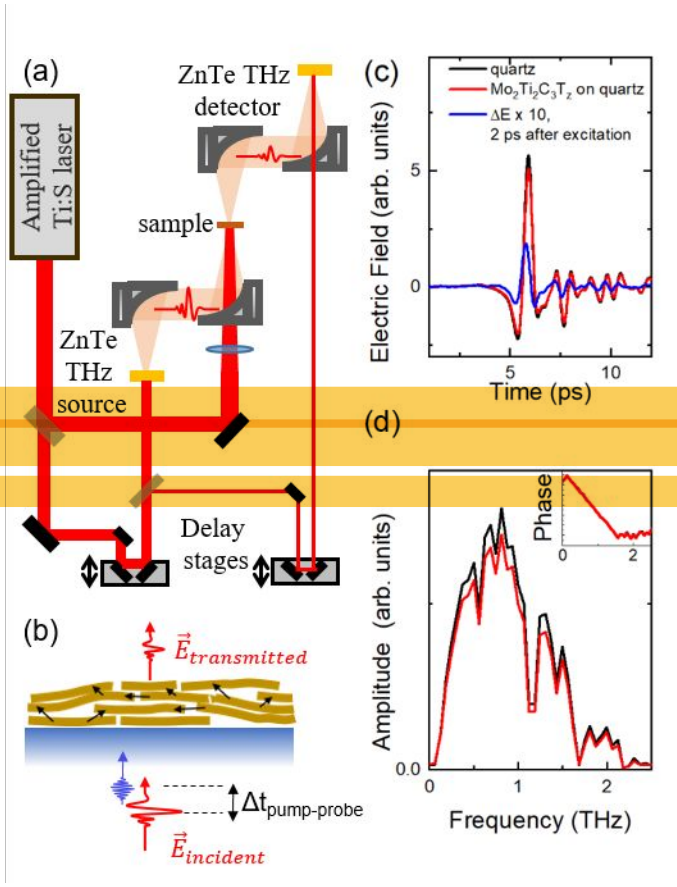

Figure 2. (a) Schematic diagram of THz TDS and TRTS. (b) Probing motion of photoexcited carriers in MXene nanosheet by THz probe pulses. (c) THz waveforms transmitted through the substrate, through a MXene film on a quartz substrate, and the photoinduced change in the transmitted waveform 2 ps after excitation with ~ 256 μJ/cm^2, 800 nm pulse. Comparing in the frequency domain the magnitude and phase (d) of THz pulses transmitted through the substrate with and without a MXene film yields a complex conductivity $\tilde{\sigma}(\omega) = \sigma_1 + i\sigma_2$

Here, we exploit the ability of THz spectroscopy to glean information about *both inter-nanosheet and intra-nanosheet* contribution to conductivity to investigate the microscopic conductivity and carrier dynamics in two Mo-based MXenes, $Mo_2Ti_2C_3T_z$ and $Mo_2TiC_2T_z$ (Figure 1 (a, b)) films. Earlier transport measurements demonstrated that intercalation of water and tetrabutylammonium cations (TBA^+) between the nanosheets that occurs during film preparation increases the inter-nanosheet spacing and electrical resistance, resulting in negative dR/dT values.[1] Vacuum annealing has been found to increase conductivity and reduce the inter-nanosheet distances by releasing some of the intercalants (Figure 1c)[1, 7]. In this study, we investigated how a mild (200 °C) vacuum anneal impacts transport properties of these two Mo-based MXenes.

One finding of this work is the dramatically different response of the Mo-based MXenes to photoexcitation compared to that of $Ti_3C_2T_z$. Unlike $Ti_3C_2T_z$, where optical excitation suppresses conductivity, here a long-lived positive photoconductivity in both $Mo_2Ti_2C_3T_z$ and $Mo_2TiC_2T_z$, with a lifetimes that can be increased by annealing. We hypothesize that over an order of magnitude lower intrinsic carrier density (~ 10^{20} cm^{-3} vs ~ 10^{21} cm^{-3} in $Ti_3C_2T_z$) makes the inter-band carrier excitation the most pronounced effect of photoexcitation on conductivity in Mo-based MXenes. These findings highlight the broad range of optoelectronic properties of metallic MXenes, where substituting Ti for Mo at some of the transition metal sites and changing the inter-layer spacing by annealing can also be used to engineer the transient photoconductive response.

2. Experimental Details.

2a. Samples

The MAX powders were made by mixing molybdenum, Mo, (-325 mesh, Alfa Aesar), titanium, Ti, (-325 mesh, Alfa Aesar), aluminum, Al, (-325 mesh, Alfa Aesar) and graphite, C, (-300 mesh, Alfa

Aesar), powders in a molar ratio (Mo:Ti:Al:C) of 2:1:1.1:2 and 2:2:1.1:2.8 for Mo_2TiAlC_2 and $Mo_2Ti_2AlC_3$, respectively. The mixed powders were ball milled using zirconia balls in plastic containers for 24 h at 70 rpm and then heated under flowing argon (Ar) at 1600 °C for 4 h. The heating and cooling rates were set at 5°C/min. The resulting loosely sintered blocks were ground using a milling bit on a drill press and the resulting powders passed through a 400 mesh (particle size < 38 μm) sieve to use for further experiments[19]. To etch the resulting MAX phases, 1 g of sieved MAX powders was slowly added to 10 ml of 50% HF solution and stirred for 72 h at 55°C and 500 rpm. The resulting slurry was transferred into a 50 mL centrifuge tube and DI water was added to completely fill the remaining volume. It was then centrifuged at 3500 rpm for 60 s and the resulting clear supernatant discarded after which the washing was repeated until the pH of the solution was ≈ 7.

To aid in the dispersion of the nanosheets one ml of 1.5 M tetrabutylammonium hydroxide, TBAOH, solution is added to the resulting sediment. The mixture was then shaken using a vortex shaker for 0.5 h. Then 200 proof ethanol, EtOH, was added to fill the remaining volume of the centrifuge tube and shaken for 120 s and later centrifuged at 3500 rpm for 60 s. The clear EtOH supernatant was then discarded and the process was repeated 2 more times. EtOH is used because it prevents the MXene nanosheets from deflocculating and washes away any excess TBAOH. After the last wash, the EtOH was discarded and 30 ml of DI water was added to the MXene slurry which was then hand shaken for 0.5 h to form a MXene colloidal suspension. To separate the non-delaminated multilayer MXene and unetched MAX phase particles, the colloid is centrifuged at 3500 rpm for 0.5 h and the supernatant is stored for further use.

For the THz measurements, a ~ 80 nm thick film of $Mo_2Ti_2C_3T_z$ was spin-coated onto on 1 mm thick quartz substrates (Figure S1). XRD patterns of this film showed that the d-spacing between nanosheets was 3.2 nm. Since we could not produce a high enough colloid concentration for the $Mo_2TiC_2T_z$ composition for spin coating, in this case a film was produced by drop-casting the colloidal suspension directly onto a quartz substrate to yield a thicker (~ 1300 nm, Figure S1) film that XRD indicated contained some un-reacted Ti_3AlC_2 (see Figure S3). The optical absorption coefficient (Figure S2) for this composition is lower than that for $Mo_2Ti_2C_3T_z$. Samples were cut in half, and one part of each sample was annealed for 12 h in vacuum (< 20 mTorr) at 200 °C. To understand the effect annealing on the films, XRD patterns were obtained after annealing and compared to those before annealing. Figure S3 shows that upon annealing the d-spacing of the $Mo_2Ti_2C_3T_z$ sample decreased from 3.2 nm to 2.0 nm. The results for the $Mo_2TiC_2T_z$ films were more ambiguous.

2b. THz Spectroscopy.

THz spectroscopy measurements were carried out as described previously and illustrated schematically in Figure. 2.[15, 26-27] In brief, ps-long THz pulses with the bandwidth between 0.25-2.2 THz (1-9 meV) are generated by optical rectification of 100 fs, 800 nm pulses in a 1 mm thick [110] ZnTe crystal. The pulse were focused onto the sample using off-axis parabolic mirrors (Figure 2(a)). At normal incidence, the THz pulses probe conductivity parallel to the substrate, and therefore mainly in the basal plane of the nanosheets comprising the MXene films (Fig. 2(b)), which is of particular interest as transport in MXenes is predominantly two dimensional.[31]

Transmitted THz pulses are detected using free-space electro-optic sampling in a second 1 mm thick [110] ZnTe crystal.

In THz TDS, coherent detection of the amplitude and phase of THz probe pulses (Fig. 2(c)) in the time domain allows for the extraction of a sample's frequency-dependent complex conductivity by comparing, in the frequency domain, the amplitudes and phases of the THz pulses transmitted through the substrate alone and the sample on the substrate (Fig. 2(d)). All experiments were carried out at ambient conditions with humidity in the 30-60% range. The series of dips in the THz amplitude spectrum (Fig. 2d) represents absorption by atmospheric water vapor.[32] To account for frequency-dependent variation of THz probe amplitude, all fits of THz spectra discussed below were weighted by the corresponding THz amplitude spectrum.

To investigate the effects of optical excitation on the conductivity of our films, we used 800 nm (or 1.55 eV), 100 fs pulses as the optical pump, and detected the photo-induced changes in the complex THz conductivity using a time-delayed THz probe pulse. As the low energy THz pulses are absorbed by the free, mobile carriers in the films, we probe the impact of the photoexcitation on the conductivity by following the optical pump – induced changes in the THz absorption as a function of optical pump – THz probe delay. In fact, in the limit of small photo-induced changes, the negative change in the transmission of the THz probe pulse peak is proportional to the transient change in the conductivity, or the photoconductivity, since $\Delta T(t)/T \propto \Delta\sigma(t)$.

3. Results and Discussion

3a. THz TDS: intrinsic microscopic conductivity

Complex, frequency-resolved THz conductivity for both MXenes before and after a mild, 200 °C, anneal in vacuum are shown in Fig. 3. First, comparison of the magnitude of the real conductivity (σ_1, solid symbols) reveals *that increase in the fraction of Mo correlates with increased conductivity in MXene films*, an observation that is consistent with DC electronic measurements[1, 31]. Analysis of the spectral shape of complex frequency-resolved conductivity yields additional information about the microscopic conductivity and contributions of intra-nanosheet and inter-nanosheet transport.

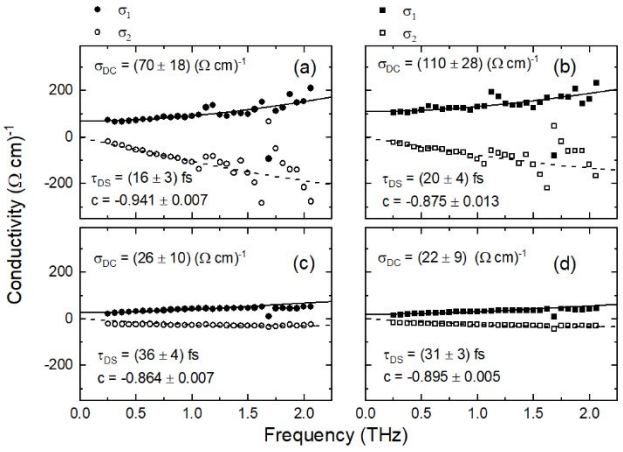

Figure 3. TDS of $Mo_2Ti_2C_3T_z$, (a) as deposited and (b) after a mild 200 °C vacuum annealing. (c) same as (a) but for $Mo_2TiC_2T_z$, (d) same as (b) but for $Mo_2TiC_2T_z$. Solid symbols represent real, and open symbols – imaginary conductivity, with lines showing global fits of both the real and imaginary conductivity to the Drude-Smith model (Eq. 1) with parameters σ_{DC}, τ_{DS} and c indicated on individual panels.

We model the complex conductivity with a phenomenological Drude-Smith model, a modification of the free carrier Drude conductivity that accounts for localization of the mobile carriers on length scales commensurate with their mean

free path, such as *localization within individual nanosheets.*[27, 33-41] Complex frequency-resolved conductivity is given as $\tilde{\sigma}(\omega) = \frac{\sigma_0}{1 - i\omega\tau_{DS}}\left(1 + \frac{c}{1 - i\omega\tau_{DS}}\right)$, where τ_{DS} is a carrier relaxation time, $\sigma_0 = \frac{Ne^2\tau_{DS}}{m^*}$, N is the intrinsic charge carrier density and m^* is the carrier effective mass. In this formalism, the DC conductivity is given by $\sigma_{DC} = \sigma_0(1 + c)$, where c is a phenomenological parameter that is a measure of carrier localization over the probed length scales. When $c = 0$, the system is fully percolated and carriers move throughout the sample unimpeded. For $c = -1$, the σ_{DC} is suppressed as the carriers are localized over short distances. In the case of MXene films, tested herein, the c-parameter can be interpreted as a measure of inter-nanosheet transport, and the long-range conductivity in the DC limit is expressed by the equation given above.

Short-range carrier mobility within the nanosheets can be calculated as $\mu_{short-range} = \frac{e\tau_{DS}}{m^*}$ if m* is known, and the long-range mobility is then given as $\mu_{long-range} = \mu_{short-range}(1 + c)$. Lines in Figure 3 represent global fits of both the real and imaginary conductivity component to the Drude-Smith model with fitting parameters σ_{DC}, τ_{DS}, and c indicated on the individual panels. Intrinsic THz conductivity measured by the TDS shows that both $Mo_2Ti_2C_3T_z$ and $Mo_2TiC_2T_z$ have considerable densities of free, delocalized carriers that attenuate the THz probe pulses via free carrier absorption. As the carrier effective mass in these MXenes is yet to be determined, we assume here that m* = m_e, for the purposes of comparing intrinsic carrier densities and mobilities and elucidating the effects of annealing on those parameters. This approximation also assumes that the carrier effective mass is similar in both compositions. With these assumptions, we estimate that intrinsic carrier densities to be ~ 2.5×10^{20} cm^{-3} for $Mo_2Ti_2C_3T_z$ and ~ 0.2×10^{20} cm^{-3} for $Mo_2TiC_2T_z$. While these values are over an order of magnitude lower compared to $Ti_3C_2T_z$ films,[15, 18] they are still significantly high, consistent with the metallic nature of these MXenes.[1, 7]

Given that the c-parameter is close to -1 and the real conductivity component decreases at lower frequencies, it is reasonable to conclude that the materials' nanosheets edges have a detrimental effect on the long-range conductivity. Such suppression of the real conductivity at lower frequencies is a hallmark of a system where grain boundaries or potential fluctuations impede long range carrier transport, and is observed in many granular and nanostructured materials.[33-34, 41-43]

Again assuming $m^* \approx m_e$, we estimate that intrinsic, intra-nanosheet mobility in $Mo_2Ti_2C_3T_z$ is $\mu_{short-range}$~ 30 cm^2/Vs, while the long-range, inter-nanosheet mobility is ~ 17 times lower. Likewise, for $Mo_2TiC_2T_z$, $\mu_{short-range}$~ 60 cm^2/Vs, and long-range mobility is ~ 8 times lower. This observation of the inter-nanosheet transport being strongly impeded agrees well with our previous conclusion – viz. VRH and thermally-activated hopping inter-nanosheet transport being rate-limiting - reached from analysis of temperature-dependent conventional DC conductivity measurements.[1] We also find that despite a shorter relaxation time and a stronger suppression of inter-nanosheet conductivity, $Mo_2Ti_2C_3T_z$ is more conductive compared to $Mo_2TiC_2T_z$, owing to a higher free carrier density. Along the same lines DFT calculations on $Mo_2Ti_3C_2O_2$ and $Mo_2TiC_2O_2$, indicate that the DOS at E_F in the latter is ≈ 3 times higher than the former consistent with the conclusions reached herein. We note in passing that DFT predicts that only O-terminated Mo-

based MXenes are metallic. Others are predicted to have small band gaps, for which little evidence is found herein or elsewhere.[3]

Intriguingly, at ~ 30 cm^2/Vs, the intrinsic conductivity of $Mo_2Ti_2C_3T_z$ is half that of $Mo_2TiC_2T_z$. To explain this observation we refer to a recent XPS study of the Mo-based MXenes explored here[44], where we concluded that: i) The Ti atoms that substitute for Mo in the outer layers are dissolved during the etching procedure, and ii) the fraction of Ti in the Mo layers is higher in $Mo_2Ti_2C_3T_z$ than in $Mo_2TiC_2T_z$. It follows that the fraction of vacant sites in the Mo-layers is higher in $Mo_2Ti_2C_3T_z$, which may very well explain why the intrinsic mobility in the latter is only half the former. Recall that the DOS at E_F for MXenes in general and for the Mo-based MXenes in particular is comprised mostly of Mo d-d orbitals[3] and hence any defects in those layers would have a disproportionate effect on mobilities.

Lastly in this section, we find that mild (200 °C) annealing of the films in vacuum, which is thought to reduce inter-nanosheet distances by removing water and other species that become intercalated between the MXene layer, almost doubles the intrinsic conductivity in a $Mo_2Ti_2C_3T_z$ film but has a minimal effect on intrinsic THz conductivity in $Mo_2TiC_2T_z$ one. From XRD diffraction of the $Mo_2Ti_2C_3T_z$ films before and after annealing (Figure. S3) we find that the d-spacing decreases from 3.2 nm to 2.0 nm. This change is consistent with the increase in conductivity observed upon annealing. For reasons that are not clear the XRD patterns of the $Mo_2Ti_2C_3T_z$ films before and after annealing were more ambiguous (see Figure S3) and did not allow us to reach any conclusions concerning their interlayer spacings. However, given that in this case there was little change in conductivity, whatever changes in d spacings, if any, did not alter the conductivity much.

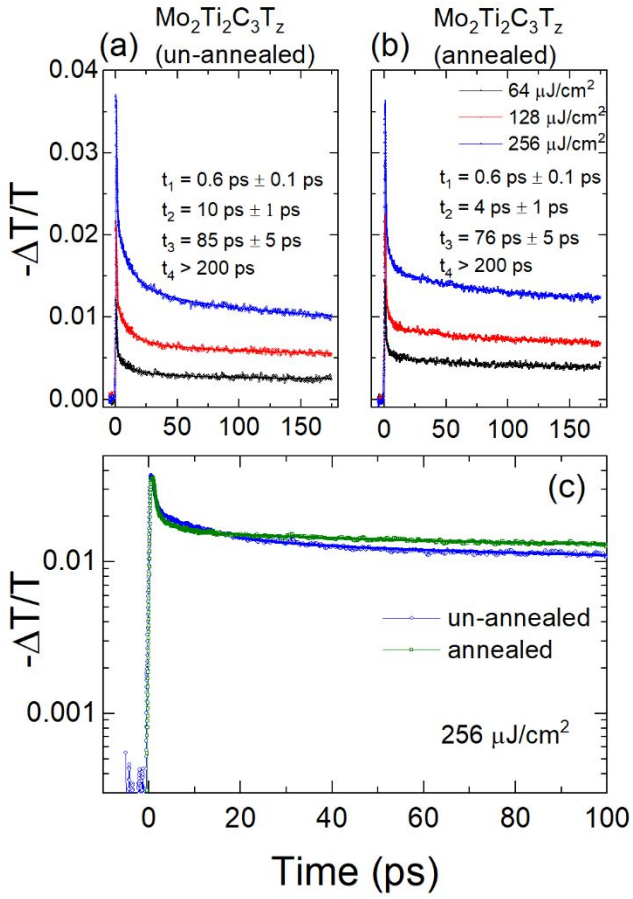

Figure 4. Transient photoconductivity in $Mo_2Ti_2C_3T_z$ ($-\Delta T/T \propto \Delta\sigma$): photoconductivity decays following excitation with 800 nm, 100 fs pulses with different fluence values, as indicated in the legend, for (a) un-annealed, as-deposited film and (b) film annealed in vacuum at 200°C. Experimental data are fitted to a multi-exponential decay, and resulting decay times, which are fluence-independent, are given in panels. (c) Comparison of the transient photoconductivity decay for un-annealed and annealed films.

3b. Time-resolved THz spectroscopy: effect of photoexcitation on microscopic conductivity

The transient photoconductivity dynamics after photoexcitation with 800 nm, 100 fs pulses are summarized in Figures 4 and 5 for $Mo_2Ti_2C_3T_z$, and $Mo_2TiC_2T_z$ films, respectively. The first important observation is *the positive sign of the transient conductivity change* in both films, in stark contrast to our previous results for the metallic $Ti_3C_2T_z$, which exhibited a photo-induced suppression of conductivity.[15] Both $Mo_2Ti_2C_3T_z$ and

$Mo_2TiC_2T_z$ are intrinsically metallic, albeit with a lower free carrier density. This transient increase in conductivity in response to optical excitation suggests that inter-band excitations inject a new population of free carriers (electrons and holes) into delocalized states above (or below, in the case of holes) E_F.

The following observations are salient:

- Just like for the intrinsic conductivity, the observed photoconductivity peak immediately after optical excitation is higher in $Mo_2Ti_2C_3T_z$ than $Mo_2TiC_2T_z$. At the same excitation fluence (256 μJ/cm^2), change in transmission of the THz pulse peak is nearly three times stronger despite the thickness of the film being significantly smaller in the $Mo_2Ti_2C_3T_z$ case. In both films, the optical penetration depth at 800 nm is comparable to the film thickness (Figure S2), and most of the 800 nm pump is absorbed over the film's thickness. Therefore, lower observed peak photoconductivity in $Mo_2TiC_2T_z$ suggests that a large fraction of photo-injected free carriers are trapped, or recombine, over time scales that are beyond the time resolution of our measurements, viz.< 200 fs.

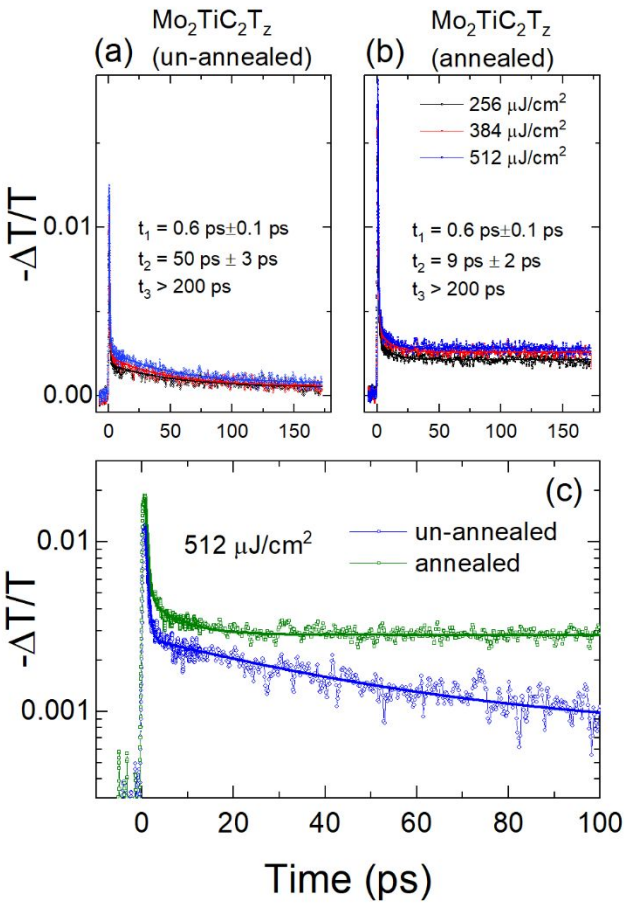

Figure 5. Transient photoconductivity in $Mo_2TiC_2T_z$ ($-\Delta T/T \propto \Delta\sigma$): photoconductivity decays following excitation with 800 nm, 100 fs pulses with different fluence values, as indicated in legends, for (a) un-annealed, as-deposited film and (b) film annealed in vacuum at 200°C. Same fluence values were used in (a) and (b), given in a legend in (b). Experimental data are fitted to a multi-exponential decay, and resulting decay times are given in the graphs. (c) Comparison of the transient photoconductivity decay for un-annealed and annealed films.

- Just like for the intrinsic conductivity, the observed photoconductivity peak immediately after optical excitation is higher in $Mo_2Ti_2C_3T_z$ than $Mo_2TiC_2T_z$. At the same excitation fluence (256 μJ/cm^2), change in transmission of the THz pulse peak is nearly three times stronger despite the thickness of the film being significantly smaller in the $Mo_2Ti_2C_3T_z$ case. In both films, the optical penetration depth at 800 nm is comparable to the film thickness (Figure S2), and most of the 800 nm pump is absorbed over the film's thickness. Therefore, lower observed peak photoconductivity in $Mo_2TiC_2T_z$ suggests that a large fraction of photo-injected free carriers are trapped, or recombine, over time scales that are beyond the time resolution of our measurements, viz.< 200 fs.

- In both films, peak photoconductivity immediately after excitation is followed by a multi-exponential decay, presumably, as the photoinjected free carriers recombine, thermalize with the intrinsic carriers or become trapped by defects.

- In both samples, at t_1~ 0.6 ps, the fastest decay component is quite fast. It becomes more pronounced with increased excitation fluence (and thus number of optically injected free carrier density) and is un-affected by annealing. We therefore ascribe it to rapid, carrier

density-dependent processes such as carrier-carrier scattering and, possibly, Auger recombination.

- In $Mo_2Ti_2C_3T_z$, we resolve three more decay slower components, one on the order of ps, another, on the order of tens of ps, and a significantly slower one (> 200 ps) that we cannot measure accurately as it extends well beyond our time range. The specific decay times are not affected by the excitation fluence in the studied range, and the contribution of the individual exponential components scale linearly with the fluence. In $Mo_2TiC_2T_z$, two more decay components are observed, in addition to the aforementioned 0.6 ps decay. One of them decays over tens of ps, the other – over > 200 ps. It is reasonable to expect that similar carrier relaxation and trapping processes are present in both materials; in this case, the relaxation process that we do not directly observe in $Mo_2TiC_2T_z$ may occur over a much shorter time scale, beyond our experimental time resolution.
- Overall, when we compare the photoconductivity decays for the un-annealed films, we find that the photoexcited excess free carriers remain delocalized for much longer in $Mo_2Ti_2C_3T_z$, with a photoconductivity at 100 ps after the excitation at nearly a third of its peak value. In the $Mo_2TiC_2T_z$ film, that value is < 10 % which suggests a higher density of defect trap states that can efficiently capture photoexcited free carriers in this film.

  Lastly in this section, we observe that annealing at 200°C, which has previously been shown to remove water molecules and TBA^+ ions trapped between the nanosheets in the film and decrease the inter-nanosheet distance,[1, 7] has only a minor effect on the magnitude of photoconductivity but leads to significant changes in the photoconductivity *dynamics and free carrier lifetime*. In both films, decay times of the processes that occur over ps to tens of ps shorten, while the slowest component (> 200 ps) becomes more pronounced, as can be seen particularly clearly in the semi-log plots in Figures 4(c) and 5(c). The changes are much more dramatic in the case of $Mo_2TiC_2T_z$, however.

These results beg the questions: What processes are responsible for the observed photoconductivity dynamics, and why does the annealing have these effects? Before answering these questions, we can gain additional insight by analyzing the frequency-resolved, complex photoinduced conductivity at different times after optical excitation, within the Drude-Smith formalism. In TRTS, the unexcited sample serves as a reference. The photoconductivity spectra at a specific time after photoexcitation provide a snapshot of the optically-excited changes to the microscopic conductivity due to inter-band excitation of new carriers as well

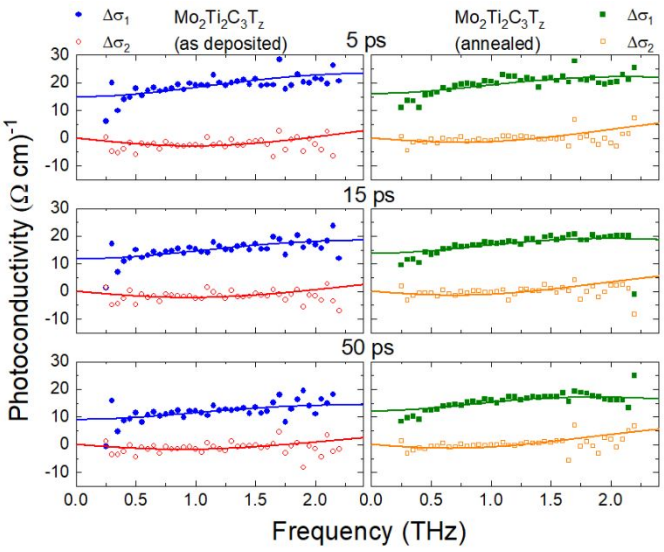

Figure 6. Photoinduced change in complex THz conductivity in $Mo_2Ti_2C_3T_z$ at different times after excitation with excitation with ~ 256 μJ/cm², 100 fs, 800 nm pulses for an un-annealed (left) and annealed (right) films. Solid and open symbols show real and imaginary conductivity components, respectively. Lines are fits of experimental data to Drude-Smith model.

as the changes in mobility of existing carriers by intra-band excitation and thermalization between the intrinsic and photoinjected carriers. The photo-conductivity spectra at three different times (5 ps, 15 ps, and 50 ps) after excitation for $Mo_2Ti_2C_3T_z$ films are shown in Fig. 6. The results are shown before annealing (left panels) and after (right panels in Fig. 6). Figure 7 shows the photoconductivity spectra at three times (3 ps, 5 ps, and 20 ps) for the un-annealed and annealed $Mo_2TiC_2T_z$ films.

For both MXenes, the shape of the photoconductivity spectra are quite different from the intrinsic conductivity and exhibit less suppression of the real component at low frequencies. The scattering time and the c-parameters obtained by fitting the experimental data to the Drude-Smith model capture this difference. The 1.55 eV excitation creates a population of free carriers (electrons and holes) that have longer scattering time compared to the intrinsic free carriers and experience a less negative c-parameter (-0.67 vs -0.94 for the un-annealed $Mo_2Ti_2C_3T_z$ film, and -0.75 vs -0.86 for $Mo_2TiC_2T_z$ film), demonstrating *the higher long-range, inter-nanosheet mobility* compared to the intrinsic free carriers (Table 1). This suggests that an optical pulse injects a population of electrons (holes) into delocalized bands at the energies above (below) the Fermi level, E_F. We find that these extrinsic carriers are less affected by the inter-nanosheet boundaries compared to the intrinsic carriers at E_F.

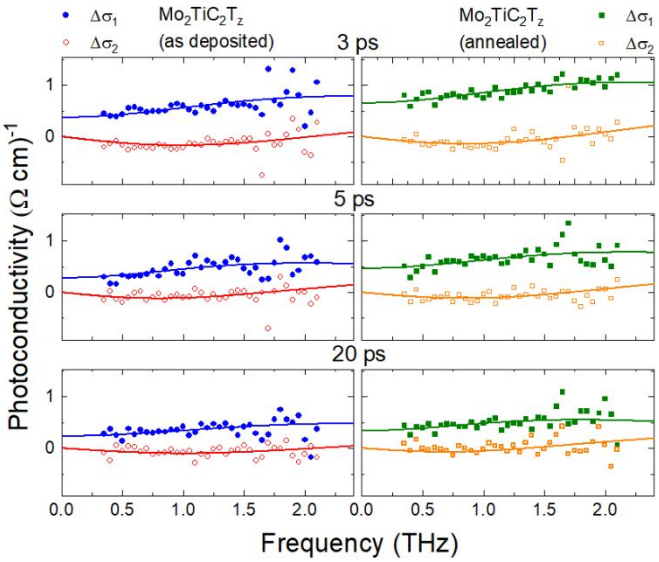

Figure 7. Photoinduced change in complex THz conductivity in $Mo_2TiC_2T_z$ at different times after excitation with excitation with ~ 512 μJ/cm², 100 fs, 800 nm pulses for an un-annealed (left) and annealed (right) films. Solid and open symbols show real, and imaginary conductivity components, respectively. Lines are fits of experimental data to Drude-Smith model.

	$Mo_2Ti_2C_3T_z$	**$Mo_2TiC_2T_z$**
Intrinsic carriers, un-annealed	-0.941±0.007	-0.864±0.013
Intrinsic carriers, annealed	-0.875±0.013	-0.895±0.005
Photoexcited carriers, un-annealed	-0.67±0.02	-0.75±0.02
Photoexcited carriers, un-annealed	-0.62±0.02	-0.69±0.02

Table 1. Drude-Smith c-parameter for intrinsic and photoexcited carriers in un-annealed and annealed $Mo_2Ti_2C_3T_z$ and $Mo_2TiC_2T_z$.

Over the time scales given by the photoconductivity dynamics (Fig. 4 and 5), those excess carriers become trapped by the available defect states, recombine and eventually relax back to the ground state.

Looking more closely at the $Mo_2Ti_2C_3T_z$ film, the magnitude of the photoinduced conductivity at 5 ps in the DC limit after photoexcitation with a 256 μJ/cm^2 pulse is nearly one third of the magnitude of the intrinsic conductivity and changes little up to 50 ps after photoexcitation. At the same time, the excess carrier density, estimated from the Drude-Smith fitting with m^* approximated by m_e, is only ~1% of the intrinsic carrier density at ~ 10^{18} cm^{-3}. This observation underscores that optically injected carriers have higher short-range, intra-nanosheet, as well as long-range, inter-nanosheet, mobility and therefore contribute significantly more to conductivity. Annealing causes subtle changes in the spectral shape. Fitting the data to the Drude-Smith model, we find that annealing result in a small but detectable increase in the c-parameter experienced by the photoexcited carriers from 0.67±0.02 to -0.62±0.02. This implies that, like for the intrinsic carriers, *annealing enhances intra-nanosheet transport for photoexcited carriers.* This results presumably from the reduced intra-nanosheet spacing as confirmed by XRD diffraction. The scattering time (and therefore the average photoexcited carrier mobility) varies between ~ 75 fs to ~ 50 fs with time and excitation (Fig. 8).

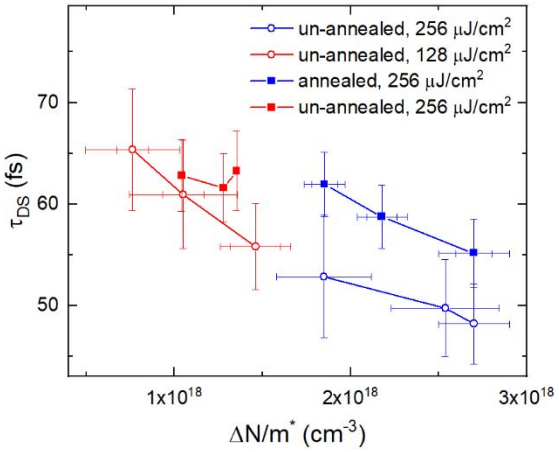

Figure 8. Scattering time τ_{DS} as a function of photoexcited carrier density in $Mo_2Ti_2C_3T_z$ scaled by the effective mass, extracted by fitting the complex photoconductivity spectra at different times after excitation and different excitation fluence values for un-annealed (open symbols) and annealed (solid symbols) samples.

Figure 8 plots the scattering time, τ_{DS}, as a function of photoexcited carrier density scaled by the effective mass extracted from the Drude-Smith fitting of data at different times and excitation fluences. Here the scattering time increases at lower carrier densities, a hallmark that carrier-carrier scattering plays a prominent role at high carrier densities.[45-46] Annealing *increases carrier scattering time* in $Mo_2Ti_2C_3T_z$, an increase we hypothesize results from the removal of intercalated species present on surfaces of the nanosheets, which affect the motion of carries in the conductive core regions of the nanosheets by causing potential fluctuations. The combined effect of improved intra-nanosheet and inter-nanosheet carrier mobility, represented by the changes in both scattering time τ_{DS} and c-parameter, is probably responsible for improved carrier transport in annealed $Mo_2Ti_2C_3T_z$. These observed, annealing-induced, changes in mobility of free carriers and their ability to move between neighboring nanosheets may help explain changes in dynamics. If the intermediate time-scale photoconductivity decay components, ~ 10 ps and ~ 85 ps (~ 4 ps and 76 ps after annealing), represent trapping of mobile carriers by *defects near nanosheet edges*, then the higher mobility and improved inter-nanosheet transport in the annealed film facilitates it. Said otherwise, the better long-range mobility results in faster trapping of the photoinduced carriers at nanosheet boundaries. Carrier trapping and recombination at point defects *within* the individual nanosheets is likely responsible for the slowest, >200 ps, decay component which is slowed after annealing, suggesting that mild

annealing may 'heal' some of the point defects. Alternatively, annealing may lessen their deleterious effect by removing water and other intercalants from their vicinity if those species are co-located with the point defects that facilitate carrier trapping.

The photoinduced conductivity in the $Mo_2TiC_2T_z$ films (Fig. 7) is an order of magnitude smaller than in the $Mo_2Ti_2C_3T_z$ films, even at early times as presumably most photoexcited carriers recombine or become localized over very short time scales. For a small fraction of photoexcited delocalized carriers that remain after the initial fast decay, the photoconductivity spectra share many similarities with $Mo_2Ti_2C_3T_z$. Again, carrier scattering time (and therefore the intra-nanosheet mobility) is higher than that for the intrinsic free carriers (60±5 fs vs 36±4 fs). This scattering time is unchanged for different times after excitation and excitation fluence values, as the low photoinjected carrier density does not allow for a significant carrier-carrier scattering contribution. Moreover, unlike the $Mo_2Ti_2C_3T_z$ film, annealing does not significantly impact the carrier scattering time in $Mo_2TiC_2T_z$. It does, however, improve inter-nanosheet transport, as evidenced by changes in c-parameter from -0.75±0.02 to -0.69±0.02 after annealing. Again, this c-parameter is less negative than the one characterizing the intrinsic, not photoexcited, carriers, suggesting that photoexcitation generated a new population of delocalized carriers that have an easier time travelling between nanosheets. Looking back at photoconductivity dynamics (Fig. 5), annealing has a much more dramatic effect on the lifetime of photoexcited carriers in $Mo_2TiC_2T_z$ than $Mo_2Ti_2C_3T_z$, which may imply a larger density of defects both at the nanosheet edges and point defects within the nanosheets. Presumed edge trapping time reduces considerably in the annealed film, from ~ 50 ps to ~ 9 ps, as inter-nanosheet hopping is enhanced, as evidenced by the change in c-parameter. The longer time scale component is also dramatically slowed, as can be best seen in Fig. 5(c), suggesting that $Mo_2TiC_2T_z$ nanosheets are more susceptible to the deleterious effects of point defects and intercalated species on the lifetime of photoinduced carriers.

A recent XPS study on $Mo_2TiC_2T_z$ and $Mo_2Ti_2C_3T_z$ films concluded that the harsh conditions needed to etch these phases into monolayers, results in their partial oxidation[44]. The TBAOH used to delaminate the monolayers resulted in further oxidation and a reduction in the F-content. In all cases, etching resulted in a decrease in the Ti to Mo ratio and the loss of Ti also resulted in the loss of C atoms. The Ti atoms lost are presumed to be ones that had substituted for Mo in the outer layers[47]. Evidence was also presented for O substituting for C-vacancies. It follows that in the final analysis the microstructures of the films fabricated is quite complicated, which partially explains the complex transport response observed herein. Needless to add much more work, beyond the scope of this paper, is needed to fully understand the subtle interactions between electronic transport and defects in general, and point defects in particular. This comment notwithstanding, the results obtained herein are an excellent first attempt at fleshing out some of these interactions. There are few other techniques that can do that.

4. Summary and Conclusions

An overall better picture of the microscopic carrier mobility and carrier dynamics in Mo-containing MXenes emerges from the results shown herein and earlier temperature-dependent transport measurements[1]. Demonstrated previously to be metallic, individual 2D $Mo_2Ti_2C_3T_z$ and

$Mo_2TiC_2T_z$ nanosheets have high intrinsic carrier density (on the order of 10^{20} cm^{-3}). These intrinsic free carriers, as well as excess carriers injected by intra-band optical excitations, experience band-like, delocalized transport *within individual nanosheets*.

However, the inter-nanosheet boundaries strongly suppress long-range transport in these films, and long-range, inter-nanosheet mobility of intrinsic carriers is nearly an order of magnitude lower than short-range, intra-nanosheet mobility. Our results are consistent with those of Halim et al., who concluded that VRH with possibly a contribution of thermally activated transport at temperatures > 130 K, is the operative mechanism for carriers to move *between the individual 2D nanosheets*.[1]

In stark contrast to $Ti_3C_2T_z$ films where we have recently reported suppression of conductivity by optical excitation, here we find that optical excitation with 1.55 eV photons increases conductivity of both $Mo_2Ti_2C_3T_z$ and $Mo_2TiC_2T_z$ films. This enhancement occurs by injecting additional free carriers by intra-band optical excitations. Both short-range (intra-nanosheet) and long-range (inter-nanosheet) mobility is higher for the photoexcited carriers compared to the intrinsic carriers, possibly because they reside in higher energy states with different average band curvatures.

Annealing further improves short- and long-range carrier transport of photoexcited carriers in both studied films. We conjecture that trapping at point defects within the nanosheets and/or at the nanosheets edges and interfaces rapidly reduces the photoexcited carrier density within the first tens of ps, and these processes are even faster after annealing when inter-nanosheet transport is improved. However, a fraction of photoexcited carriers survive for substantially longer periods, well over 200 ps, suggesting that these carriers are confined within the nanosheets. This fraction is significantly higher in $Mo_2Ti_2C_3T_z$ than in $Mo_2TiC_2T_z$, and in both Mo-MXenes, it is increased after annealing.

In summary, Mo-based MXenes exhibit optical absorption across the visible and near-infrared range. Unlike $Ti_3C_2T_z$, where photoexcitation suppresses conductivity, the Mo-based MXenes demonstrate a high and long-lived photoinduced conductivity. These observations highlight a wide range of properties that can be achieved by engineering MXene's structure and composition. In the specific case of $Mo_2Ti_2C_3T_z$ and $Mo_2TiC_2T_z$, their properties render them attractive for a whole host of optoelectronic, sensing and photoelectrochemical applications.

Acknowledgments

We thank Dr. Thierry Ouisse for insightful discussions, Maryam Masroor Shalmani for assistance with annealing of samples, and Binod Giri for assistance with and SEM imaging. This work was funded by NSF (DMR 1740795).

References

(1) Halim, J.; Moon, E. J.; Eklund, P.; Rosen, J.; Barsoum, M. W.; Ouisse, T. Variable range hopping and thermally activated transport in molybdenum-based MXenes. *Physical Review B* **2018,** *98* (10), 104202, DOI: 10.1103/PhysRevB.98.104202.
(2) Halim, J.; Kota, S.; Lukatskaya, M. R.; Naguib, M.; Zhao, M.-Q.; Moon, E. J.; Pitock, J.; Nanda, J.; May, S. J.; Gogotsi, Y.; Barsoum, M. W. Synthesis and Characterization of 2D Molybdenum Carbide (MXene). *Adv. Funct. Mater.* **2016,** *26* (18), 3118-3127, DOI: 10.1002/adfm.201505328.
(3) Anasori, B.; Shi, C.; Moon, E. J.; Xie, Y.; Voigt, C. A.; Kent, P. R. C.; May, S. J.; Billinge, S. J. L.; Barsoum, M. W.; Gogotsi, Y. Control of electronic properties of 2D carbides (MXenes) by manipulating their transition metal layers. *Nanoscale Horizons* **2016,** *1* (3), 227-234, DOI: 10.1039/C5NH00125K.
(4) Khazaei, M.; Ranjbar, A.; Arai, M.; Yunoki, S. Topological insulators in the ordered double transition metals $M_2'M''C_2$ MXenes (M'=Mo, W; M''=Ti, Zr, Hf). *Physical Review B* **2016,** *94* (12), 125152, DOI: 10.1103/PhysRevB.94.125152.
(5) Halim, J.; Persson, I.; Moon, E. J.; Kühne, P.; Darakchieva, V.; Persson, P. O. Å.; Eklund, P.; Rosen, J.; Barsoum, M. W. Electronic and optical characterization of 2D Ti2C and Nb2C (MXene) thin films. *J. Phys.: Condens. Matter* **2019,** *31* (16), 165301, DOI: 10.1088/1361-648x/ab00a2.
(6) Khazaei, M.; Ranjbar, A.; Arai, M.; Sasaki, T.; Yunoki, S. Electronic properties and applications of MXenes: a theoretical review. *Journal of Materials Chemistry C* **2017,** *5* (10), 2488-2503, DOI: 10.1039/c7tc00140a.
(7) Hart, J. L.; Hantanasirisakul, K.; Lang, A. C.; Anasori, B.; Pinto, D.; Pivak, Y.; van Omme, J. T.; May, S. J.; Gogotsi, Y.; Taheri, M. L. Control of MXenes' electronic properties through termination and intercalation. *Nature Communications* **2019,** *10* (1), 522, DOI: 10.1038/s41467-018-08169-8.
(8) Dillon, A. D.; Ghidiu, M. J.; Krick, A. L.; Griggs, J.; May, S. J.; Gogotsi, Y.; Barsoum, M. W.; Fafarman, A. T. Highly Conductive Optical Quality Solution-Processed Films of 2D Titanium Carbide. *Adv. Funct. Mater.* **2016,** *26* (23), 4162-4168, DOI: 10.1002/adfm.201600357.
(9) Ghidiu, M.; Lukatskaya, M. R.; Zhao, M.-Q.; Gogotsi, Y.; Barsoum, M. W. Conductive two-dimensional titanium carbide 'clay' with high volumetric capacitance. *Nature* **2014,** *516*, 78, DOI: 10.1038/nature13970.
(10) Ali, A.; Belaidi, A.; Ali, S.; Helal, M. I.; Mahmoud, K. A. Transparent and conductive Ti3C2Tx (MXene) thin film fabrication by electrohydrodynamic atomization technique. *Journal of Materials Science-Materials in Electronics* **2016,** *27* (5), 5440-5445, DOI: 10.1007/s10854-016-4447-z.
(11) Dong, Y.; Chertopalov, S.; Maleski, K.; Anasori, B.; Hu, L.; Bhattacharya, S.; Rao, A. M.; Gogotsi, Y.; Mochalin, V. N.; Podila, R. Saturable Absorption in 2D Ti_3C_2 MXene Thin Films for Passive Photonic Diodes. *Adv. Mater.* **2018,** *30* (10), 1705714, DOI: doi:10.1002/adma.201705714.
(12) Han, M.; Yin, X.; Wu, H.; Hou, Z.; Song, C.; Li, X.; Zhang, L.; Cheng, L. Ti3C2 MXenes with Modified Surface for High-Performance Electromagnetic Absorption and Shielding in the X-Band. *ACS Applied Materials & Interfaces* **2016,** *8* (32), 21011-21019, DOI: 10.1021/acsami.6b06455.
(13) In, J. Y.; Joonhoi, K.; Babak, A.; Minah, S.; Han, L. J.; Yury, G.; Min, J. Y. Metallic MXene Saturable Absorber for Femtosecond Mode-Locked Lasers. *Adv. Mater.* **2017,** *29* (40), 1702496, DOI: doi:10.1002/adma.201702496.
(14) Jiang, X.; Liu, S.; Liang, W.; Luo, S.; He, Z.; Ge, Y.; Wang, H.; Cao, R.; Zhang, F.; Wen, Q.; Li, J.; Bao, Q.; Fan, D.; Zhang, H. Broadband Nonlinear Photonics in Few-Layer MXene $Ti_3C_2T_x$ (T = F, O, or OH). *Laser & Photonics Reviews* **2018,** *12* (2), 1700229, DOI: doi:10.1002/lpor.201700229.
(15) Li, G.; Kushnir, K.; Dong, Y.; Chertopalov, S.; Rao, A. M.; Mochalin, V. N.; Podila, R.; Titova, L. V. Equilibrium and non-equilibrium free carrier dynamics in 2D Ti 3 C 2 T x MXenes: THz spectroscopy study. *2D Materials* **2018,** *5* (3), 035043.
(16) Zhang, C.; Anasori, B.; Seral-Ascaso, A.; Park, S. H.; McEvoy, N.; Shmeliov, A.; Duesberg, G. S.; Coleman, J. N.; Gogotsi, Y.; Nicolosi, V. Transparent, Flexible, and Conductive 2D Titanium Carbide

(MXene) Films with High Volumetric Capacitance. *Adv. Mater.* **2017,** *29* (36), 1702678, DOI: doi:10.1002/adma.201702678.
(17) Shahzad, F.; Alhabeb, M.; Hatter, C. B.; Anasori, B.; Man Hong, S.; Koo, C. M.; Gogotsi, Y. Electromagnetic interference shielding with 2D transition metal carbides (MXenes). *Science* **2016,** *353* (6304), 1137-1140, DOI: 10.1126/science.aag2421.
(18) Miranda, A.; Halim, J.; Barsoum, M. W.; Lorke, A. Electronic properties of freestanding $Ti_3C_2T_x$ MXene monolayers. *Appl. Phys. Lett.* **2016,** *108* (3), 033102, DOI: 10.1063/1.4939971.
(19) Anasori, B.; Xie, Y.; Beidaghi, M.; Lu, J.; Hosler, B. C.; Hultman, L.; Kent, P. R. C.; Gogotsi, Y.; Barsoum, M. W. Two-Dimensional, Ordered, Double Transition Metals Carbides (MXenes). *ACS Nano* **2015,** *9* (10), 9507-9516, DOI: 10.1021/acsnano.5b03591.
(20) Jepsen, P. U.; Cooke, D. G.; Koch, M. Terahertz spectroscopy and imaging–Modern techniques and applications. *Laser & Photonics Reviews* **2011,** *5* (1), 124-166.
(21) Baxter, J. B.; Guglietta, G. W. Terahertz spectroscopy. *Anal. Chem.* **2011,** *83* (12), 4342-68, DOI: 10.1021/ac200907z.
(22) Cunningham, P. D.; McCreary, K. M.; Hanbicki, A. T.; Currie, M.; Jonker, B. T.; Hayden, L. M. Charge Trapping and Exciton Dynamics in Large-Area CVD Grown MoS2. *The Journal of Physical Chemistry C* **2016,** *120* (10), 5819-5826, DOI: 10.1021/acs.jpcc.6b00647.
(23) Cunningham, P. D.; Hayden, L. M.; Yip, H. L.; Jen, A. K. Y. Charge Carrier Dynamics in Metalated Polymers Investigated by Optical-Pump Terahertz-Probe Spectroscopy. *J. Phys. Chem. B* **2009,** *113* (47), 15427-15432, DOI: 10.1021/jp906454g.
(24) Laforge, J. M.; Cocker, T. L.; Beaudry, A. L.; Cui, K.; Tucker, R. T.; Taschuk, M. T.; Hegmann, F. A.; Brett, M. J. Conductivity control of as-grown branched indium tin oxide nanowire networks. *Nanotechnology* **2014,** *25* (3), 035701, DOI: 10.1088/0957-4484/25/3/035701.
(25) Ulbricht, R.; Hendry, E.; Shan, J.; Heinz, T. F.; Bonn, M. Carrier dynamics in semiconductors studied with time-resolved terahertz spectroscopy. *Reviews of Modern Physics* **2011,** *83* (2), 543-586, DOI: 10.1103/RevModPhys.83.543.
(26) Butler, K. T.; Dringoli, B. J.; Zhou, L.; Rao, P. M.; Walsh, A.; Titova, L. V. Ultrafast carrier dynamics in $BiVO_4$ thin film photoanode material: interplay between free carriers, trapped carriers and low-frequency lattice vibrations. *Journal of Materials Chemistry A* **2016,** *4* (47), 18516-18523, DOI: 10.1039/C6TA07177E.
(27) Titova, L. V.; Cocker, T. L.; Xu, S.; Baribeau, J.-M.; Wu, X.; Lockwood, D. J.; Hegmann, F. A. Ultrafast carrier dynamics and the role of grain boundaries in polycrystalline silicon thin films grown by molecular beam epitaxy. *Semicond. Sci. Technol.* **2016,** *31* (10), 105017.
(28) Lloyd-Hughes, J.; Jeon, T.-I. A Review of the Terahertz Conductivity of Bulk and Nano-Materials. *Journal of Infrared, Millimeter, and Terahertz Waves* **2012,** *33* (9), 871-925, DOI: 10.1007/s10762-012-9905-y.
(29) Beard, M. C.; Turner, G. M.; Schmuttenmaer, C. A. Transient photoconductivity in GaAs as measured by time-resolved terahertz spectroscopy. *Physical Review B* **2000,** *62* (23), 15764-15777, DOI: 10.1103/PhysRevB.62.15764.
(30) Demsar, J.; Dekorsy, T. Carrier dynamics in bulk semiconductors and metals after ultrashort pulse excitation. In *Optical Techniques for Solid-State Materials Characterization*; 2016; pp 291-328.
(31) Ouisse, T.; Barsoum, M. W. Magnetotransport in the MAX phases and their 2D derivatives: MXenes. *Materials Research Letters* **2017,** *5* (6), 365-378, DOI: 10.1080/21663831.2017.1333537.
(32) Xin, X.; Altan, H.; Saint, A.; Matten, D.; Alfano, R. R. Terahertz absorption spectrum of para and ortho water vapors at different humidities at room temperature. *J. Appl. Phys.* **2006,** *100* (9), 094905, DOI: 10.1063/1.2357412.

(33) Cocker, T. L.; Titova, L. V.; Fourmaux, S.; Bandulet, H. C.; Brassard, D.; Kieffer, J. C.; El Khakani, M. A.; Hegmann, F. A. Terahertz conductivity of the metal-insulator transition in a nanogranular VO_2 film. *Appl. Phys. Lett.* **2010,** *97* (22), DOI: 10.1063/1.3518482.
(34) Cocker, T. L.; Baillie, D.; Buruma, M.; Titova, L. V.; Sydora, R. D.; Marsiglio, F.; Hegmann, F. A. Microscopic origin of the Drude-Smith model. *Physical Review B* **2017,** *96* (20), 205439, DOI: 10.1103/PhysRevB.96.205439.
(35) Jensen, S. A.; Ulbricht, R.; Narita, A.; Feng, X.; Mullen, K.; Hertel, T.; Turchinovich, D.; Bonn, M. Ultrafast photoconductivity of graphene nanoribbons and carbon nanotubes. *Nano Lett.* **2013,** *13* (12), 5925-30, DOI: 10.1021/nl402978s.
(36) Guglietta, G. W.; Diroll, B. T.; Gaulding, E. A.; Fordham, J. L.; Li, S.; Murray, C. B.; Baxter, J. B. Lifetime, Mobility, and Diffusion of Photoexcited Carriers in Ligand-Exchanged Lead Selenide Nanocrystal Films Measured by Time-Resolved Terahertz Spectroscopy. *Acs Nano* **2015,** *9* (2), 1820-1828, DOI: 10.1021/nn506724h.
(37) Richter, C.; Schmuttenmaer, C. A. Exciton-like trap states limit electron mobility in TiO_2 nanotubes. *Nature Nanotechnology* **2010,** *5*, 769, DOI: 10.1038/nnano.2010.196

https://www.nature.com/articles/nnano.2010.196#supplementary-information.
(38) Alberding, B. G.; DeSario, P. A.; So, C. R.; Dunkelberger, A. D.; Rolison, D. R.; Owrutsky, J. C.; Heilweil, E. J. Static and Time-Resolved Terahertz Measurements of Photoconductivity in Solution-Deposited Ruthenium Dioxide Nanofilms. *Journal of Physical Chemistry C* **2017,** *121* (7), 4037-4044, DOI: 10.1021/acs.jpcc.6b12382.
(39) Alberding, B. G.; Kushto, G. P.; Lane, P. A.; Heilweil, E. J. Reduced photoconductivity observed by time-resolved terahertz spectroscopy in metal nanofilms with and without adhesion layers. *Appl. Phys. Lett.* **2016,** *108* (22), DOI: 10.1063/1.4953208.
(40) Walther, M.; Cooke, D. G.; Sherstan, C.; Hajar, M.; Freeman, M. R.; Hegmann, F. A. Terahertz conductivity of thin gold films at the metal-insulator percolation transition. *Physical Review B* **2007,** *76* (12), DOI: 10.1103/PhysRevB.76.125408.
(41) Titova, L. V.; Cocker, T. L.; Cooke, D. G.; Wang, X.; Meldrum, A.; Hegmann, F. A. Ultrafast percolative transport dynamics in silicon nanocrystal films. *Physical Review B* **2011,** *83* (8), DOI: 10.1103/PhysRevB.83.085403.
(42) Baxter, J. B.; Schmuttenmaer, C. A. Conductivity of ZnO nanowires, nanoparticles, and thin films using time-resolved terahertz spectroscopy. *J. Phys. Chem. B* **2006,** *110* (50), 25229-25239, DOI: 10.1021/jp064399a.
(43) Cooke, D. G.; Meldrum, A.; Uhd Jepsen, P. Ultrabroadband terahertz conductivity of Si nanocrystal films. *Appl. Phys. Lett.* **2012,** *101* (21), 211107, DOI: doi:http://dx.doi.org/10.1063/1.4767145.
(44) Halim, J.; Cook, K. M.; Eklund, P.; Rosen, J.; Barsoum, M. W. XPS of cold pressed multilayered and freestanding delaminated 2D thin films of Mo2TiC2Tz and Mo2Ti2C3Tz (MXenes). *Appl. Surf. Sci.* **2019,** *494*, 1138-1147, DOI: https://doi.org/10.1016/j.apsusc.2019.07.049.
(45) Mics, Z.; D'Angio, A.; Jensen, S. A.; Bonn, M.; Turchinovich, D. Density-dependent electron scattering in photoexcited GaAs in strongly diffusive regime. *Appl. Phys. Lett.* **2013,** *102* (23), 231120, DOI: 10.1063/1.4810756.
(46) Sharma, G.; Al-Naib, I.; Hafez, H.; Morandotti, R.; Cooke, D. G.; Ozaki, T. Carrier density dependence of the nonlinear absorption of intense THz radiation in GaAs. *Opt. Express* **2012,** *20* (16), 18016-18024, DOI: 10.1364/OE.20.018016.
(47) Anasori, B.; Dahlqvist, M.; Halim, J.; Moon, E. J.; Lu, J.; Hosler, B. C.; Caspi, E. a. N.; May, S. J.; Hultman, L.; Eklund, P.; Rosén, J.; Barsoum, M. W. Experimental and theoretical characterization of ordered MAX phases Mo2TiAlC2 and Mo2Ti2AlC3. *J. Appl. Phys.* **2015,** *118* (9), 094304, DOI: 10.1063/1.4929640.